MATERIALE PLASTICE
https://revmaterialeplastice.ro
https://doi.org/10.37358/Mat.Plast.1964

Effect of Different Particle Size Hollow Microbeads on the Mechanical Diffraction Process of Epoxy Resin Composites

ZHE WU[1], HAI FENG JIANG[1], YANG ZHANG[2]*, SHUAI ZHAO[1], CHUN MEI YANG[1], QING NAN WANG[1]
[1]College of Mechanical and Electrical Engineering, Northeast Forestry University, Harbin 150040, P.O. Box 3010, No. 26, He Xing Road, China
[2]College of Science, Northeast Forestry University, Harbin, 150040, P.O. Box 3010, No. 26, He Xing Road, China

Abstract: *The industrial grade hollow beads were divided into three particle sizes of 40 mesh, 60 mesh and 80 mesh and added into the epoxy resin material matrix to prepare porous foam composites. The quasi-static compression experiments were performed on porous foam composites at room temperature, and the stress-strain curves of quasi-static compression processes were analyzed separately for different particle sizes. According to the characteristics of the compression curve of porous foam materials, the representative characteristic parameters of each stage are extracted separately. The fracture characteristics of the microscopic samples of the compressed material specimens were observed by electron microscopy, and the deformation patterns of the composite materials were analyzed. And combined with SEM pictures to analyze the form of microbead crushing and matrix pore collapse mode, according to which the particle size suitable for this matrix is 60 mesh and the mass fraction of microbeads is 10%.*

Keywords:*porous materials, mechanical testing, stress rupture, electron microscopy, fracture toughness*

1. Introduction

Epoxy Resin is a polymeric oligomer containing two or more epoxy groups and formed by the ring-opening cross-linking reaction of epoxy groups with aliphatic, alicyclic or aromatic organic compounds as bones. In recent years, with the improvement of polymer material theory and the in-depth exploration of composite material theory, more research scholars tend to use epoxy resin as the matrix, add reinforcement materials to it and through different molding processes, to obtain a wide range of composite materials with outstanding performance advantages [1-3]. At the same time, according to the present domestic and international academic results, the emergence of epoxy resin-based composites has indeed broadened the application fields of the original matrix materials. In addition, epoxy resin is widely used in the field of aerospace [4-8], construction [9-13], electrical materials [14-17] and composites [18-22].

Aaron S. Krieg et al. added acid-treated carbon nanotubes (CNTs) to aerospace-grade epoxy resin and characterized the composites, concluding that the bending strength of the composites could be increased by 10.6 MPa when the CNTs content was 0.4 wt% [23]. Nishant Shirodkar et al. investigated the effect of incorporation of carbon nanotubes and graphene nanosheets (GNPs) on the fracture toughness enhancement of the material, and showed that the fracture toughness and fracture energy of 0.5% CNT-Epoxy samples were increased by 118 and 311%, respectively [24]. In addition, surface crack deflection and some crack bifurcation can be observed in GNP epoxy samples. It is also concluded that the synergy between CNTs and GNPs in CNT / GNP epoxy samples is poor. Daisuke S. et al. studied the bending properties of short carbon fiber / epoxy resin composites, and analyzed the relationship between fiber orientation and plastic behavior of carbon fiber / epoxy resin composites [25]. The effective coefficients for the volume fraction of short fibers in composites were proposed, and the Halpin-Tsai equation was improved as a theory to predict the bending modulus. Mechin P. et al. studied the effect of nano-filler content on the compressive strength of continuous carbon fiber / epoxy resin

*email: zhangyang@nefu.edu.cn

matrix composites and mainly analyzed the relationship between compression failure mode and nano-filler content [26]. It is concluded that the failure mechanism is fiber micro bending when the content of nano-filler is the highest.

In addition, some scholars from universities in other countries have also conducted experimental studies and theoretical elaborations on the theory of particle-modified epoxy resins. Ozmen Eruslu et al. investigated the failure mechanism of glass particle-epoxy composites under compression and sliding wear, and numerical simulations of the elastic properties of the composites were performed for the bonded interfaces [27, 28]. The results were compared using the MoriTanaka mean field method, which yielded effective parameters for the debonding mechanism including matrix yield stress, plastic strain, particle penetration at the contact interface, and particle stress. Muhammad Umair et al. studied the effects of the microstructure of reinforced fabric and the addition of glass bead filler (GMS) on the drop weight impact properties of hemp / green epoxy resin composite samples [29]. The results showed that composite samples reinforced with satin weave reinforcements exhibited the highest impact force values, while composite samples containing 5% GMS exhibited higher elasticity and stiffness compared to other structures. M. Megahed et al. evaluated tthe improvement of mechanical properties by adding nano and micron aluminum particles to glass fiber reinforced epoxy resin composites [30]. The study showed that the tensile strength of the material increased by 27% with the addition of 2wt%, while the tensile elongation, toughness, tensile modulus, bending strength, bending strain and bending modulus increased by 114%, 116%, 21%, 52.2%, 21.4% and 76.6% respectively with the addition of 4wt%.

In basalt fiber (BF)/ epoxy resin (EP) composites, Yinuo Bie et al. carried out collaborative modification by nano-SiO_2 and KH560 [31]. The tensile and bending properties of BF/EP materials are improved, and the creep compliance and its growth rate are significantly reduced, and the long-term prediction of creep performance indicators is carried out by the HKK model. Ding Junjie et al. prepared hollow glass microspheres (HGM)/epoxy resin (EP) composite foam materials with epoxy resin as filler [32, 33]. The effects of HGM wall thickness and content on the density, open cell ratio and morphology of HGM preforms and HGM/EP composite foams were studied. The results show that the compressive strength has nothing to do with the wall thickness of HGM, but decreases with the increase of HGM content, but the change of compressive modulus is positively correlated with the wall thickness of HGM. Wang Shuo et al. added 4% rigid nano-SiO_2 particles to the nano-rubber particle (RnP)/epoxy resin (EP) composite material to improve the rigidity and tensile strength caused by the addition of RnP, and further increase the toughness of the epoxy resin [34]. The Young's modulus and tensile strength were increased by 28 and 23% respectively. At the same time, the thermal stability of epoxy composites was characterized by dynamic mechanical analysis and thermogravimetric analysis.

In this study, hollow microspheres/epoxy resin composites with different particle sizes were prepared and quasi-static compression tests were carried out with a universal testing machine to obtain stress-strain curves. The deformation mechanism of hollow micro-bead composites with different particle sizes at different stages of compression process is analyzed. The mechanical evolution mechanism of composites was analyzed by corresponding SEM images at different deformation stages and the reasonable mass fraction interval of hollow microspheres in composites was explored.

2. Materials and methods

2.1. Experimental materials

The Hollow fly-ash beads used in the experiment was purchased from Shanghai GREENYA Nanomaterials Co., Ltd. and part of the specifications are shown in Table 1 and Table 2.

Table 1. Performance parameters of hollow microspheres

Material name	Accumulation density (g/cm^3)	Diameter (μm)	Compressive strength (MPa)
Hollow microspheres	0.3 ~ 0.6	20 ~ 400	10 ~ 50

Table 2. Chemical composition parameters of hollow microbeads (wt%)

Al_2O_3	SiO_2	Fe_2O_3	CaO	MgO	K_2O	C	TiO_2
26～35	55～65	0.2～1	0.2～0.6	1～2	0.5～4.0	0.01～2	0.5～2

The E51 bisphenol A epoxy resin used in the experiment was purchased from Guangzhou Suixin Chemical Co., Ltd. and part of the specifications are shown in Table 3.

Table 3. Parameters of E51 bisphenol A epoxy resin

20℃ Viscosity (mpa·s)	Epoxy equivalent (g/ep)	Inorganic chlorine content(mg/kg)	Density (g/cm^3)	Softening Point (℃)
12460	186.2	48	1.36	15-23

The D230 Polyetheramine curing agent used in the experiment was purchased from Jinan Pulaihua Chemical Co., Ltd.The 1,3-Cyclohexanedimethylamine acceleratorused in the experiment was purchased from Jiangsu Minglin Chemical Co., Ltd.The Butyl glycidyl ether diluentused in the experiment was purchased from Shanghai Kaisai Chemical Co., Ltd. The above materials are all industrial grade materials and can be used without further purification.

2.2. Experimental methods

Remove the sunken broken microspheres by flotation with only the whole ones floating up. Clean and filter with anhydrous ethanol and place them in a vacuum drying tank at 80℃ for drying. Butyl glycidyl ether active diluent, hollow beads cleaned and dried, and polyether amine D230 curing agent and 1, 3-cyclohexanedimethylamine accelerator are added in turn to the beaker. Place beaker on magnetic stirrer and add a small amount of GP330 defoamer. Set stirring temperature to 60℃ and stirring time to 5 min. Place the beaker in a low temperature environment to increase the matrix viscosity and quickly cool to room temperature before removing. Apply the appropriate thickness of wax or cover with polyester film to the inside of the mould, and inject the epoxy resin mixed evenly with the filler into the mould, then pre-cure the sample at room temperature for 24~36 h to release the model. The WDW universal testing machine was employed to conduct the compressive tests for the specimen of different mass fractions. The compressive tests were carried out at a nominal strain rate of $10^{-3}s^{-1}$. The sample is quenched in liquid nitrogen and the quenched surface is treated by spraying gold. The section shape is observed by SEM analyzer at 12.5 kV acceleration voltage. The cross-section micro-characteristics of hollow micro-beads/epoxy resin composites and the fracture interface properties of the curing system of the blend of hollow micro-beads and epoxy resin and additives were analyzed.

2.3. Experimental equipment

The universal testing machine used in the test is WDW-100, which is produced in Changchun Kexin company. The scanning electron microscope adopts the EM-30Plus model produced by COEXM company. The device has a resolution of 5 nm and a magnification of 20 to 150,000 times. The DZF vacuum drying oven is produced by Shanghai Yiheng Technology Instrument Co., Ltd. and DF-101 heat collecting magnetic mixer is purchased from Gongyi Kerui Instrument Co., Ltd.

3. Results and discussions

3.1.Mechanical curve analysis and microstructure analysis of 40 mesh particle size hollow microbead content

A total of six specimens were used in the compression experiments, and the mass ratio of epoxy resin to curing agent was A:B = 3:1. The particle size of hollow beads is 40 mesh 250~350μm, the content

interval is set to 0% ~25%, the sampling interval is 5 % and the numbers are 0~5 respectively. The final mechanical property influence diagrams are shown in Figures 1 and Figure 2.

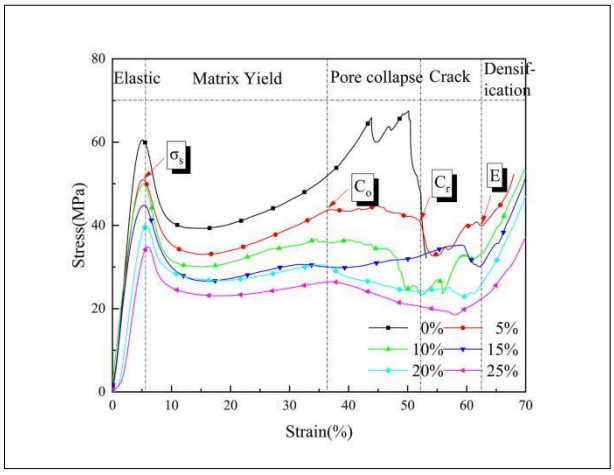

Figure 1. Stress-strain curve of different mass fractions of 40 mesh size hollow bead composite

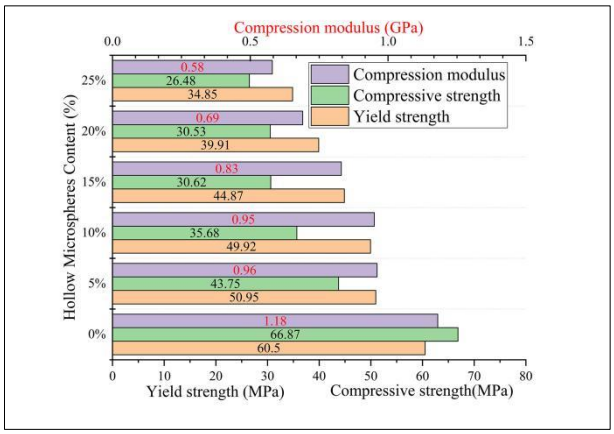

Figure 2. 40 mesh particle size hollow bead composite strength and elastic modulus bar graph

After the addition of 40 mesh hollow beads, the sampling data of specimens 1~5 basically conform to the typical trend of quasi-static compression curve of porous composites. Taking specimen 1 as an example, the curve can be further divided into five stages according to the trend characteristics, namely, elastic stage, matrix yielding stage, pore collapse stage, crushing stage and densification stage.

The elastic stage is the first stage experienced by porous composites, and the stress and strain in this stage basically show a linear relationship and end at the first maximum point: the yield point stress σ_s. The strain at the yield point position is generally between 4 and 6%.

The matrix yielding stage and the pore collapse stage are both plastic deformation stages of the material. The trend of the overall yielding phase curve is decreasing and then increasing until the end of the second maximum point, i.e., the collapse point C_0. The reason for the formation of this stage is mainly related to the yielding phenomenon of the epoxy resin matrix, while the surface of the microbeads will start to produce cracks due to the extrusion of the matrix. When the material is in the pore collapse stage, the growth trend of stress slows down or even shows a slow decline. This phenomenon is mainly due to the exposure of pores left by the occupancy effect after the massive fragmentation of microbeads. These pores will continuously collapse and deform under stress and absorb energy, so that the strain increases when the stress instead appears to decrease until the end of the breaking point C_r. After entering the crushing stage, there will be a significant drop in stress. This is because after the material has undergone

the process of internal pore collapse, the hollow spherical shell will no longer support the internal pores and will begin to gradually fall off, with some cracks growing from the inside to the surface of the substrate, thus triggering the fragmentation of the specimen as a whole. When the material continues to be compressed, the above-mentioned pores and cracks will be healed due to the coarsening of the matrix, and the material will reach the densification point E. Thereafter, the stresses will exhibit the same deformation strengthening phenomena as in a normal bulk matrix, leading to a dense phase and strain hardening phenomena.

Table 4 is obtained by extracting and plotting key data points from Figure 1 and Figure 2. Where ε_p is used to denote the total strain during the plastic deformation interval, characterizing the effective strain value of the energy absorption process of the porous foam material prior to material fragmentation. φ_c denotes the collapse strain ratio and represents the proportion of the strain value in the hole collapse stage of the material in the whole plastic deformation stage. ε_t denotes the total strain during the crushing interval, characterizing the strain value of the material from the beginning to the end of crushing. $\overline{\sigma_p}$ denotes the average value of stress in the plastic deformation interval, characterizing the average level of stress in the total process of plastic deformation energy absorption. S_p^2 denotes the stress variance within the plastic deformation interval, characterizing the stress dispersion of the energy absorption process. $\overline{\sigma_c}$ denotes the average value of stress in the pore collapse stage, characterizing the average level of stress in the pore collapse energy absorption process. S_c^2 denotes the stress variance of the pore collapse phase, characterizing the stress dispersion of the pore collapse energy absorption process. The formula for ε_p, ε_t, $\overline{\sigma_p}$, S_p^2, $\overline{\sigma_c}$, φ_c, S_c^2 is shown:

$$\varepsilon_p = \varepsilon_{cr} - \varepsilon_s \tag{1}$$

$$\varphi_c = \frac{\varepsilon_{cr} - \varepsilon_{co}}{\varepsilon_{cr} - \varepsilon_s} \tag{2}$$

$$\varepsilon_t = \varepsilon_E - \varepsilon_{cr} \tag{3}$$

$$\overline{\sigma_p} = \frac{1}{n}(\sigma_1 + \cdots + \sigma_n) \tag{4}$$

$$S_p^{\ 2} = \frac{\sum_{i=1}^{n}\left(\sigma_i - \overline{\sigma}\right)^2}{n-1} \tag{5}$$

$$\overline{\sigma_c} = \frac{1}{n}(\sigma_{c1} + \cdots + \sigma_{cn}) \tag{6}$$

$$S_c^{\ 2} = \frac{\sum_{i=1}^{n}\left(\sigma_{ci} - \overline{\sigma_c}\right)^2}{n-1} \tag{7}$$

In the formula: ε_s is yield point strain value, ε_{co} is strain value of the Collapse point C_o, ε_{cr} is the strain value of breakage point C_r, σ_1 to σ_n are the plastic deformation interval discrete point stress value, σ_{c1} to σ_{cn} are the pore collapse stage interval discrete point stress value.

When the hollow beads are not added, the matrix material lacks the pore collapse stage, and only the crushing point does not exist, and the collapse point C_o and densification point E. In Table 4 no longer give the micro bead mass fraction 0% with the value of ε_t, $\overline{\sigma_p}$, φ_c, and S_c^2 use the horizontal line instead. When the micro bead content exceeds 15%, there is no obvious division between the pore slumping

stage and the crushing stage, so the same horizontal line is used instead for ε_t with 20 and 25% micro bead content.

Table 4. Characteristic parameters in stress-strain curves for different microbead contents at 40 mesh

Bead mass fraction	ε_p	φ_c	ε_t	$\overline{\sigma_p}$	S_p^2	$\overline{\sigma_c}$	S_c^2
	(%)	(%)	(%)	(MPa)	(MPa^2)	(MPa)	(MPa^2)
0%	45.05	—	—	49.09	80.13	—	—
5%	46.87	16.49	17.53	39.43	19.57	43.35	0.74
10%	41.00	28.39	14.77	34.27	13.00	35.68	0.44
15%	53.73	51.05	2.99	30.75	10.48	31.69	2.97
20%	51.17	42.72	—	27.69	6.82	26.21	3.82
25%	50.25	37.77	—	24.03	5.80	22.68	5.04

Figure 3 shows the results of five different ratios of compressed specimens selected and photographed by bench-top scanning electron microscopy after quenching the surface treatment by liquid nitrogen. The shooting period was obtained after natural rebound for one week after compression to 70% strain, and the shooting location was chosen as the crack area at the boundary of each specimen, with a magnification of 200x.

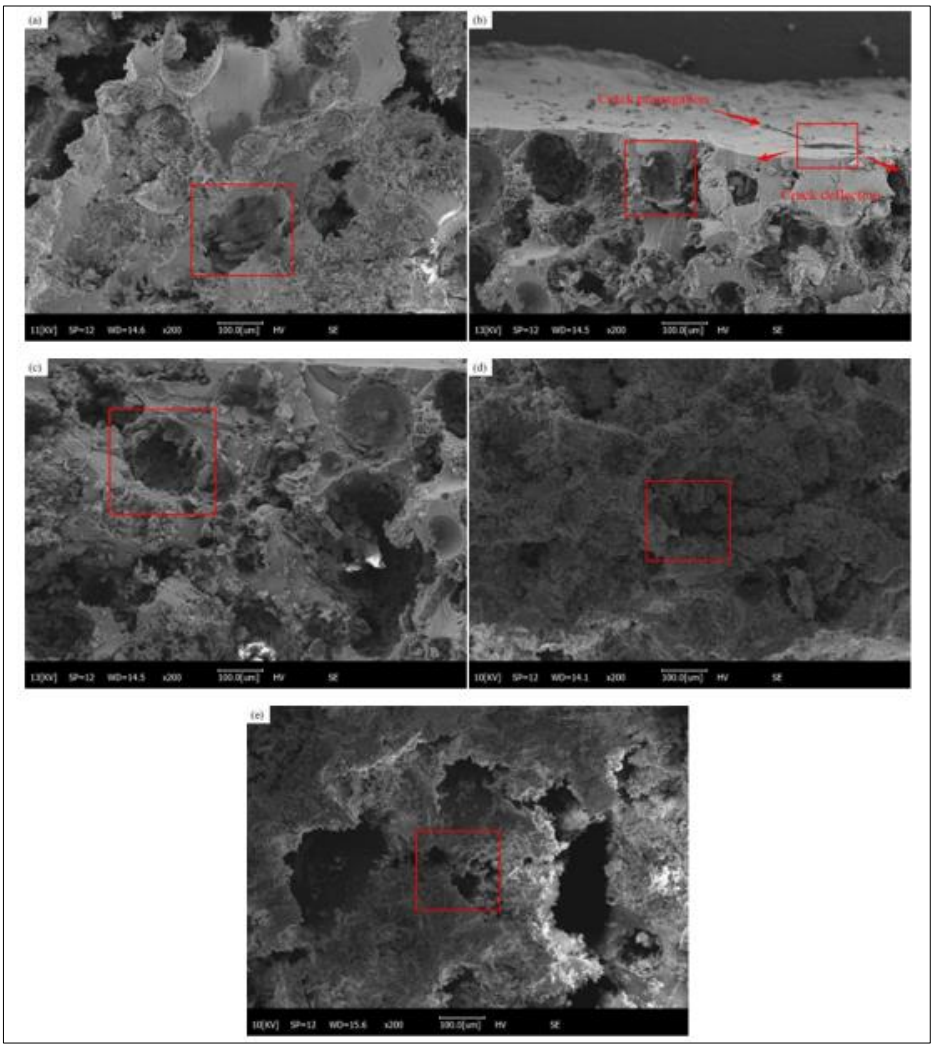

Figure 3. Microstructure diagram of different bead mass fraction of 40 mesh particle size (5%-a, 10%-b, 15%-c, 20%-d, 25%-e)

According to the overall view of Figure 3, due to the higher particle size of 40 mesh hollow microbeads, this makes the occupancy effect more obvious, and the pore diameter formed in the matrix through the occupancy effect is larger. After the material has gone through the dense stage, the fragments of the broken microbeads are partially retained in the original cavity. Further observation of the connection between the microbeads and the substrate shows that the separation interface is relatively smooth and shows flaky flaking, which is because the combination effect of hollow microbeads as inorganic filler and organic resin is slightly poor, and also shows that the combination strength of the two interfaces is not high. Meanwhile, Figure 3b also demonstrates that hollow microbeads, as a kind of granular second phase body, can also deflect cracks to a certain extent during the crack transfer process. At the same time, due to the larger particle size of the microbeads, the single crack deflection angle produced is larger and the crack deflection effect is more obvious. In addition, the epoxy resin matrix as a polymer material, the cross-linking reaction of the matrix formed itself with a certain elasticity of the vesicles. Therefore, before the matrix material is compressed to 70% strain, the material will naturally rebound under the action of internal stress, and the previously compacted internal pores will recover part of their roundness and appear elliptical-like pores.

When the content of 40 mesh beads increases, it can be seen that the size of the hollow bead fragments left in the cavity is gradually decreasing. When the microbead content is 5%, the cavity still retains the long strip shape formed by the original crack sprouting and thus cutting the microbeads. When the bead content is 10%, the fragmentation phenomenon of hollow beads is more obvious, showing polygonal shape with smaller size. When the microbead content exceeds 15%, basically no longer can you see the obvious large pieces of hollow microbead fragments, more often become powder adhering to the surface of the broken substrate. At the same time, the increase of microbead content also reduces the rebound effect of the material after densification. As shown in Figure 3b, the pores of materials with low microbead content have better roundness recovery phenomenon after rebounding, while the pore rebound shape of materials with high microbead content is closer to wedge shape in Figure 3e. The reason for the above phenomenon is that the matrix can bear more external load when the microbead content is less. When the overall strength of the material is high, it is more likely to produce rapid cracking of the microbead shell under low strain and high stress to form long straight cracks, and the bonding interface will also quickly debond and fall off into the cavity. It is not easy to compact all the voids in the dense stage, some of the pores will remain in this long strip of microbead fragments, the rebound effect of the material is more obvious, and the pores are close to elliptical after rebound. And when the content of microbeads is more, more external load needs to be borne by microbeads, and the overall strength of the material has a significant decrease. Under the relatively low stress state, the crushing speed of the microbead shell will also be slowed down, the interface debonding speed will be reduced, and the cracks will be more uniform, thus forming block fragments. It is easier to be compacted in the dense stage thus crushing the micro-bead fragments to form a powder, and the material has poorer resilience and the pores are closer to the spindle shape after rebound.

3.2. Mechanical curve analysis and microstructure analysis of 60 mesh particle size hollow microbead content

A total of six specimens were used in the compression experiments, and the mass ratio of epoxy resin to curing agent was A:B = 3:1. The particle size of hollow beads is 60 mesh 150 ~ 250μm, the content interval is set to 0% ~ 25%, the sampling interval is 5 % and the numbers are 0 ~ 5 respectively. The final mechanical property influence diagrams are shown in Figures 4 and Figure 5.

After the addition of 60 mesh hollow beads, the curves plotted by the sampling data of specimens 1 ~ 5 are similar to the curves with the addition of 40 mesh hollow beads, and the compression stages of the material are basically the same.

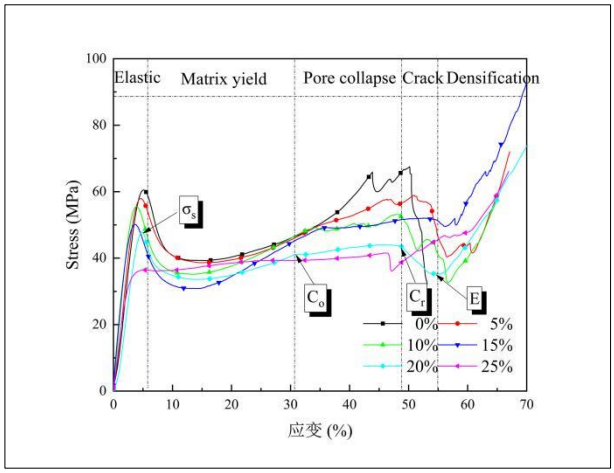

Figure 4. Stress-strain curve of different mass fractions of 60 mesh size hollow bead composite

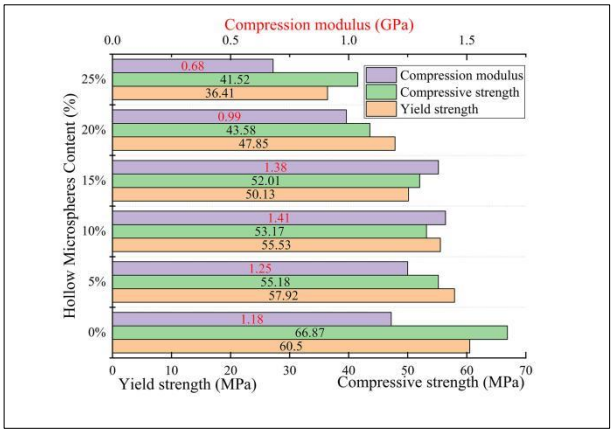

Figure 5. 60 mesh particle size hollow bead composite strength and elastic modulus bar graph

Table 5. Characteristic parameters in stress-strain curves for different microbead contents at 60 mesh

Bead mass fraction	ε_p	φ_c	ε_t	$\overline{\sigma_p}$	S_p^2	$\overline{\sigma_c}$	S_c^2
	(%)	(%)	(%)	(MPa)	(MPa^2)	(MPa)	(MPa^2)
0%	45.05	—	—	49.09	80.13	—	—
5%	47.28	15.36	6.93	47.59	48.17	57.18	0.65
10%	44.15	31.74	8.68	43.72	36.72	49.93	1.80
15%	48.99	33.87	5.42	42.47	37.43	50.32	1.14
20%	43.85	40.45	6.58	39.07	14.87	42.77	1.10
25%	40.85	52.76	0.95	38.75	2.18	39.88	0.44

Table 5 is obtained by extracting and plotting key data points from Figure 4 and Figure 5. Combining Figure 4 and 5 with Table 5 in general, the influence of mechanical properties after the addition of 60 mesh hollow microbeads and the trend of the characteristic parameters of the curve have the following characteristics:

-with the increase of microbead content, the yield strength and compression strength of the material still maintain the decreasing trend, while the modulus of elasticity first increases and then decreases, but the decreasing trend is a bit smoother than that of the 40 mesh. When the microbead content reaches 25%, the yield strength of the material appears to be less than the compression strength;

-with the increase of microbead content, the total strain ε_p in the plastic deformation interval basically shows a trend of first increasing and then decreasing, reaching a great value of 48.99% when the microbead content is 15%, while the collapse strain ratio φ_c shows a rapid increasing trend. Compared to the 40-item tier, ε_p has a smaller trend of change and φ_c has a larger trend of change. And the total strain in the crushing interval showed a trend of increasing first and then decreasing, reaching a great value of 8.68% at 10% of microbeads;

-with the increase of microbead content, the mean value of stress $\overline{\sigma_p}$ in the plastic deformation interval and the mean value of stress $\overline{\sigma_c}$ in the pore collapse stage still maintain a decreasing trend. The stress variance S_p^2 in the plastic deformation interval also shows a relatively obvious decrease, while the

stress variance S_c^2 in the pore collapse stage appears to increase first and then decrease, and the extreme value appears at 10% of the microbead content at this time;

- with the increase of the microbead content, the stress value corresponding to the densification point E decreases rapidly, the strain value decreases rapidly, and the slope of the curve in the densification stage remains basically the same.

In the elastic stage, the compressive strength of 60 mesh beads is less than the matrix strength, but it is improved compared with 40 mesh beads. Therefore, the overall yield strength of the material decreases, but the decreasing trend is much slower. At the same time, the stiffness of the microbeads themselves is increased due to the increase in relative wall thickness. After adding a small amount of 60 mesh microbeads to the matrix, the overall elastic modulus of the material will first increase with the increase of microbead content. However, as the bead content continues to increase, the spacing between the beads is shortened, and the phenomenon of poor surface resin coating will occur at some locations due to the tight accumulation of beads. At the same time, too many occupied cavities also further weaken the internal structure of the material, which in turn makes the modulus of elasticity begin to gradually decline, but the overall effect on the modulus of elasticity is not significant from the numerical point of view.

In the plastic deformation stage, 60 mesh beads weaken the mechanical properties of the substrate less than 40 mesh beads. Due to the collapse of the pore space between the microbeads and the matrix, the specific gravity of the phenomenon of stress reduction is reduced, the mechanical curve in the plastic deformation interval only appears to slow down the increase, and there is no obvious downward trend like after adding 40 mesh microbeads. The overall stress mean value $\overline{\sigma_p}$ and stress variance S_c^2 of the interval are decreased. And the advantage is that the addition of 60 mesh beads will increase the value of $\overline{\sigma_p}$ by about 10 MPa compared with 40 mesh beads under the same mass ratio.

In the pore collapse stage, the pore structure formed by 60 mesh beads is significantly more stable than that formed by 40 mesh beads after crushing. The most intuitive manifestation of this is that while the slump strain ratio φ_c is increasing at the same mass percentage, the average value of stress $\overline{\sigma_c}$ in the pore slumping stage is increased by more than 15 MPa, and the stress variance S_c^2 is relatively small. This also shows that the slumping speed of 60 mesh beads is relatively low at the same mass ratio, and the overall slumping process is relatively gentle and the phenomenon of rapid slumping of the beads has not yet occurred.

In the matrix crushing stage, 60 mesh beads also exhibit particle toughening properties of epoxy resin. Compared with 40 mesh beads, the material with 60 mesh beads has higher ε_p and lower ε_t when the content of beads is less than 15% in a side-by-side comparison. It indicates that the plastic deformation interval of the material accounts for more and the crushing interval accounts for less after the particle size is reduced, and the failure form of the material is more inclined to deformation failure. When the content of microbeads continues to increase 60 mesh microbeads, due to the structural advantage, the pore collapse stage and matrix crushing stage are clearly separated in the mass ratio of 0% to 25%, and there is no phenomenon of bubble pore and matrix crushing at the same time.

In the dense reinforcement stage, the pore diameter of 60 mesh beads is smaller than that of 40 mesh beads, so the porosity of the matrix will be reduced, which also makes the dense point of 60 mesh beads relatively leftward at the same mass ratio. However, the difference between the properties of the two materials in the dense stage is not significant, so the slopes of the curves are similar.

Figure 6 shows the results of five different ratios of compressed specimens selected and photographed by bench-top scanning electron microscopy after quenching the surface treatment by liquid nitrogen. The shooting period was obtained after natural rebound for one week after compression to 70% strain, and the shooting location was chosen as the crack area at the boundary of each specimen, with a magnification of 200x.

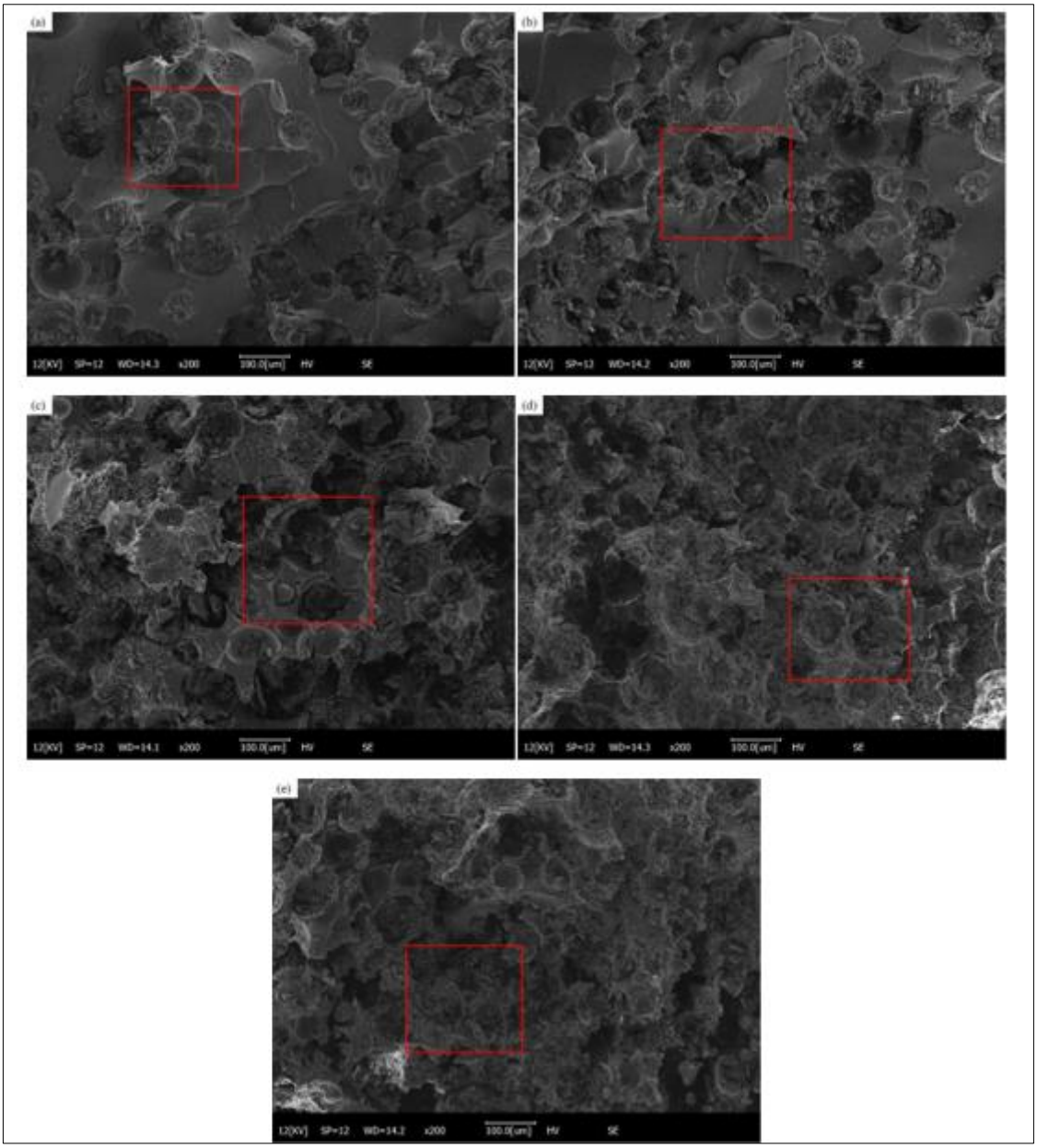

Figure 6. Microstructure diagram of different bead mass fraction of 60 mesh particle size (5%-a, 10%-b, 15%-c, 20%-d, 25%-e)

According to the overall view of Figure 6, because the particle size of 60 mesh beads is lower than that of 40 mesh beads, the distribution of beads is also more uniform, and the pore diameter formed in the matrix through the occupancy effect is more suitable. After compressing the specimens mixed with both particle size to 70% strain and rebounding naturally for one week, the recovery of roundness of 60 mesh microporosity was more obvious with the same mass ratio. This also shows that a proper reduction of hole diameter can effectively improve the compression stability performance and recovery performance of the hole structure.

In addition, according to the SEM pictures, the overall size of the fragments after the crushing of 60 mesh microbeads is smaller than that of 40 mesh microbead fragments, so that more energy can be absorbed through the crushing of the microbeads. The average pore spacing is larger at low microbead content, and the stress effect between adjacent pores is smaller, so the obvious pore boundary morphological features are still retained after rebound. At the same time, with the increase of microbead content the vesicle spacing decreases, the multi-axial stress state of the vesicle boundary is more complicated

under the two stages of pore collapse and natural rebound. The adjacent hole wall is more prone to shear, twist and other damage so that the hole wall is broken, thus losing part of the resilient energy of the material. There is an extreme value of the content of bearing microbeads in the matrix, so that the matrix has a large porosity and at the same time has a stable pore collapse performance. Take 60 mesh beads as an example, the pore shape recovery is good when the mass ratio is lower than 15%, but when the mass ratio reaches 25%, the phenomenon of bubble hole crushing has appeared. In the case of 40 mesh beads, the phenomenon of continuous crushing of bubble holes can be seen in some positions when the mass ratio is 5%, and this phenomenon becomes more and more serious as the content increases, and when the mass ratio reaches 25%, no obvious hole structure can be found. It can also be seen that the stability of the bubble pore boundary structure will increase with the decrease of the microbead size and decrease with the increase of the microbead content at a certain microbead size.

3.3. Mechanical curve analysis and microstructure analysis of 80 mesh particle size hollow microbead content

A total of six specimens were used in the compression experiments, and the mass ratio of epoxy resin to curing agent was A:B = 3:1. The particle size of hollow beads is 80 mesh 50~150μm, the content interval is set to 0% ~25%, the sampling interval is 5 % and the numbers are 0~5 respectively. The final mechanical property influence diagrams are shown in Figures 7 and Figure 8.

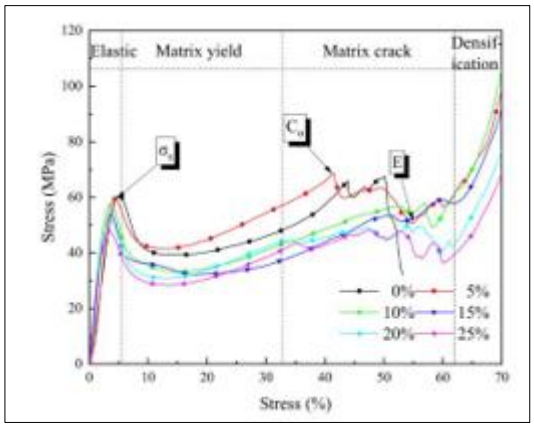

Figure 7. Stress-strain curve of different mass strength and elastic modulus bar graph

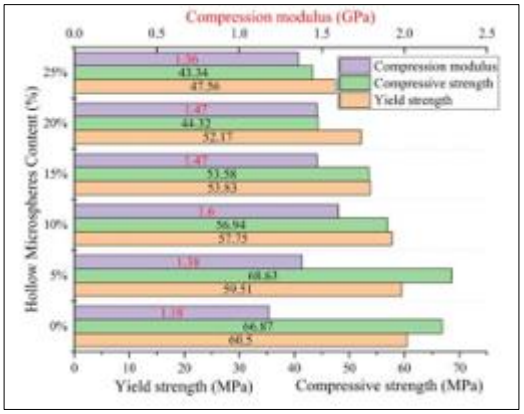

Figure 8. 80 mesh particle size hollow bead composite fractions of 80 mesh size hollow bead composite

After the addition of 80 mesh hollow beads, the curves plotted by the sampling data of specimens 1~5 were different from those with the addition of the first two kinds of beads, mainly showing that the pore collapse stage and crushing stage were not clearly divided and the stress fluctuation was larger.

Finally, after adding 80 mesh microbeads, the pore collapse stage and matrix crushing stage in the deformation stage are combined to represent the overall damage stage, and the rest of the stages are expressed in the same way. In addition, ε'_p denotes the total overall deformation strain, representing the combined strain between the yield phase and the damage phase; φ'_c denotes the damage strain ratio, representing the strain value in the damage phase of the material as a percentage of the overall deformation phase; $\overline{\sigma'_p}$ indicates the average value of stress in the overall deformation interval, representing the average level of stress in the total process of overall deformation energy absorption; S'^2_p denotes the stress variance within the plastic deformation interval, representing the stress dispersion of the energy absorption process; $\overline{\sigma'_c}$ denotes the average value of stress during the damage phase of the material, representing the average level of stress during the energy absorption of the material damage;

$S_c'^2$ denotes the stress variance of the pore collapse phase, representing the stress dispersion of the material damage energy absorption process.

Table 6. Characteristic parameters in stress-strain curves for different microbead contents at 80 mesh

Bead mass fraction	ε_p'	φ_c'	$\overline{\sigma_p'}$	$S_p'^2$	$\overline{\sigma_c'}$	$S_c'^2$
	(%)	(%)	(MPa)	(MPa^2)	(MPa)	(MPa^2)
0%	45.05	—	49.09	80.13	—	—
5%	50.50	26.55	53.33	66.32	60.25	13.86
10%	54.68	10.81	44.21	69.36	55.07	4.59
15%	58.27	19.63	42.30	76.03	55.06	7.96
20%	58.17	48.82	41.20	42.92	46.01	4.87
25%	56.55	44.14	38.44	38.40	44.05	7.83

Table 6 is extracted from the key data points in Figure 7 and plotted into a table to obtain. Combined with Figure 7 and Table 6 in general, the influence of mechanical properties after the addition of 80 mesh hollow microbeads and the trend of the characteristic parameters of the curve have the following characteristics:

-with the increase of microbead content, the yield strength of the material still maintains the decreasing trend. But the decreasing trend is more moderate than 40 mesh and 60 mesh level and the compression strength even increases first and then decreases. The modulus of elasticity is similar to the trend of 60 mesh hierarchy, and it increases first and then decreases, but the trend of increase is faster and the trend of decrease is slower.

-with the increase of the content of micro-beads, the total strain ε'_p of the whole deformation still shows the trend of first increasing and then decreasing. When the content of micro-beads is 15%, the maximum value is reached, and the failure strain ratio φ'_c also shows a fluctuating upward trend.

-as the content of micro-beads increases, the stress mean $\overline{\sigma'_p}$ in the whole deformation range and the stress mean $\overline{\sigma'_c}$ in the failure stage of the material still decrease, but the trend is more stable than that of 40 mesh and 60 mesh. The stress variance $S_p'^2$ increases first and then decreases in the whole deformation range, reaching its maximum at 15%, while the stress variance SS fluctuates and decreases at the stage of material failure.

-with the increase of microbead content, the stress value corresponding to the densification point *E* decreases slightly, the strain value increases, and the slope of the curve in the densification stage remains basically the same.

Figure 9 shows the compressed specimens of hollow bead composites with different content of 80 mesh particle size, after quenching the surface treatment by liquid nitrogen and photographed by desktop scanning electron microscope. The shooting period is obtained after compression to 70% strain by natural rebound for one week, and the shooting position is selected for each specimen boundary crack area, and the magnification is 500x.

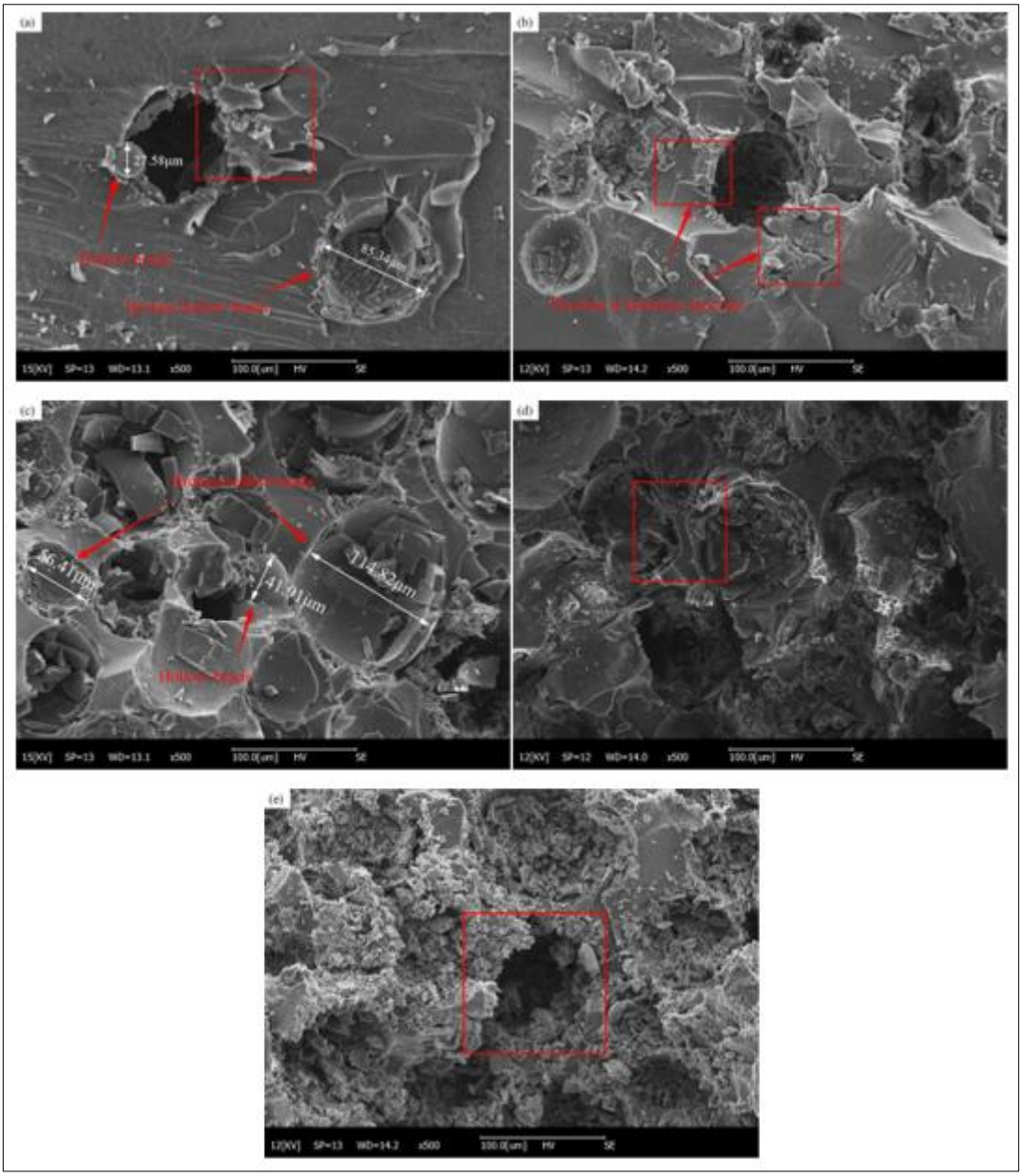

Figure 9. Microstructure diagram of different bead mass fraction of 80 mesh particle size (5%-a, 10%-b, 15%-c, 20%-d, 25%-e)

According to the overall view of Figure 9, the micropores formed by 80 mesh microbeads are basically less than 100μm. The particle size of 80 mesh beads is lower than the first two types of beads, and the pore spacing of 80 mesh bead system is significantly smaller than the first two systems under the same mass ratio. After the specimens mixed with different particle size were compressed to 70% strain and naturally rebounded for one week, the roundness of 80 mesh microporous pores with the same mass ratio had the best recovery effect and the pore structure morphology was retained most completely. It has been demonstrated that reducing the pore diameter can effectively improve the compression stability and recovery performance of the pore structure. At the same time, the 80 mesh bead system can still maintain a good pore structure morphology after the mass ratio reaches 20%, which indicates that the matrix will have a higher bearing capacity for 80 mesh beads compared with the first two systems.

According to Figure 9b, a more obvious matrix rupture occurs at the bonding interface under the 80-mesh level with the pore structure intact. This indicates a local stress concentration that exceeds the compressive strength of the matrix and eventually leads to the rupture of the matrix at that location. And

according to Figure 9a and Figure 9c, the crushing phenomenon is more obvious for the microbeads with larger particle size under the 80 mesh. The minimum particle size of microbeads broken in the figure is 56.41μm, while the maximum particle size of microbeads retained is 41.91μm, which can be seen that the particle size that makes the microbeads not broken should be below 50μm. In the process of material compression, the deformation of the microbeads at these locations is not large and due to the stress generated by elastic deformation, it starts to squeeze the surrounding matrix and microporous, resulting in cracks and breakage at adjacent locations in priority. When the higher the content of microbeads, the weakening effect on the strength of the matrix is higher. The higher the retention rate of these low particle size beads and the higher the value of the maximum retained particle size, the higher the retention rate of these low particle size beads when the stress cannot continue to rise. Therefore, it is more likely to have extrusion cracking of the substrate, thus making the stress fluctuation in the platform stage more obvious.

4. Conclusions

Properly reducing the particle size of hollow microspheres can effectively improve the compression stability and recovery performance of the structure. However, when the particle size of hollow beads is too low, it is difficult to break the beads, resulting in low utilization of pore collapse. The matrix and the low particle size microbeads produce extrusion cracks which increase the stress variance in the plastic deformation stage and make the stress fluctuation phenomenon in the platform stage more obvious.

Among the three particle sizes of hollow microspheres/epoxy resin composites, the 60-mesh particle size of hollow microspheres makes the decrease rate of stress mean value of the material most obvious during plastic deformation stage. Thus, the degree of deformation dither of the composite foam material is reduced and the stability of the composite foam material is improved.

In 60-mesh hollow microsphere/epoxy resin composites with different mass fractions, the stress mean of composites with 10% mass fraction decreases more smoothly and their energy absorption effect is better.

Acknowledgements: This material is based upon work supported by the Fundamental Research Funds for the Central Universities (grant no. 2572015CB10), the National Natural Science Foundation of China (grant no. 31200434 and 52105434).

Reference

1.MEMON, H., WEI, Y., ZHU, C., Correlating the Thermomechanical Properties of a Novel Bio-based Epoxy Vitrimer with its Crosslink Density, Mater Today Commun, 29, 2021, 102814.
2.TAHERI, M., JAHANFAR, M., OGINO, K., Cathodic Disbonding Behavior of Epoxy -Polyamide Coating, Eng Fail Anal, 130, 2021, 105740.
3.ZIHAN, W., PEIBIN, K., TIANYU, W., DONGLI, C., XIAOPING, Y., GANG, S., Atomistic Understanding of Cross-linking Network in Different Epoxy Resin: Effect of Loop Structure, Polymer, 243, 2022, 124629.
4.PERRET, B., SCHARTEL, B., STÖß, K., CIESIELSKI, M., DIEDERICHS, J., DÖRING, M., KRÄMER, J., ALTSTÄDT, V., Novel DOPO-based Flame Retardants in High-performance Carbon Fibre Epoxy Composites for Aviation, Eur Polym J, 47, 2011, 1081-1089.
5.TORRES-HERRADOR, F., ESCHENBACHER, A., COHEUR, J., BLONDEAU, J., MAGIN, T. E., VAN GEEM, K. M., Decomposition of Carbon/phenolic Composites for Aerospace Heatshields: Detailed Speciation of Phenolic Resin Pyrolysis Products, Aerosp Sci Technol, 119, 2021, 107079.
6.ARENA, M., VERTUCCIO, L., BARRA, G., VISCARDI, M., GUADAGNO, L., Damping Assessment of New Multifunctional Epoxy Resin for Aerospace Structures, Mat T Proceed, 34, 2021, 180-183.

7.LIU, Y., WILKINSON, A., Rheological Percolation Behaviour and Fracture Properties of Nano-composites of MWCNTs and a Highly Crosslinked Aerospace-grade Epoxy Resin System, Compos Part A-Appl S, 105, 2018, 97-107.
8.TENG, N., DAI, J., WANG, S., LIU, X., HU, J., YI, X., LIU, X., Hyperbranched Flame Retardant to Simultaneously Improve the Fire-safety, Toughness and Glass Transition Temperature of Epoxy Resin, Eur Polym J, 157, 2021, 110638.
9.YAGI, M., OKAWA, T., KAWANO, F., Data on Bond Strength of Resin Cement Systems to CAD/CAM Resin Composite After Aging, DATA BRIEF, 39, 2021, 107474.
10.WANG, Y., LIU, Q., Investigation on Fundamental Properties and Chemical Characterization of Water-soluble Epoxy Resin Modified Cement Grout, Constr Build Mater, 299, 2021, 123877.
11.ZHIQIANG, X., JUNCONG, W., HONGCHANG, W., Mechanics Property Analysis for A New Steel Bridge Deck Pavement with UTAC-UHPC, Forest Engineering, 36, 2020, 76-84.
12.WANG, X., MA, B., WEI, K., ZHANG, W., Thermal Stability and Mechanical Properties of Epoxy Resin/microcapsule Composite Phase Change Materials, Constr Build Mater, 312, 2021, 125392.
13.RUAN, K., ZHONG, X., SHI, X., DANG, J., GU, J., Liquid Crystal Epoxy Resins with High Intrinsic Thermal Conductivities and Their Composites: A mini-review, Mater Today Phys, 20, 2021, 100456.
14.X, W. J., C, T., ZHANG, D, T., Thermal Conductivity and Electrical Property of Epoxy Composites Mixed with Boron Nitride and Zinc Oxide Whisker Online First Acta Materiae Compositae Sinica, 37(06), 2020, 1285-1294.
15.QIAN, Y., TAO, Y., LI, W., LI, Y., XU, T., HAO, J., JIANG, Q., LUO, Y., YANG, J., High Electro-magnetic Wave Absorption and Thermal Management Performance in 3D CNF@C-Ni/epoxy Resin Composites, Chem Eng J, 425, 2021, 131608.
16.DUAN, H., WANG, X., XIE, G., HU, R., MA, H., Effect of Thermosetting Resin Matrix on Resistance-temperature Stability of Carbon Fiber Conductive Composites, Mater Res Express, 6, 2018, 015312.
17.PANG, X., WANG, R., WEI, Q., ZHOU, J., Effect of Epoxy Resin Sealing on Corrosion Resistance of Arc Spraying Aluminium Coating Using Cathode Electrophoresis Method, Mater Res Express, 5, 2018, 016527.
18.SU, Z., XI, X., HU, Y., FEI, Q., U, S., LI, H., YANG, J., A new Al_2O_3 porous ceramic prepared by addition of hollow spheres, J Porous Mat, 21, 2014, 601-609.
19.DENG, Z., YUE, J., HUANG, Z., Solvothermal Degradation and Reuse of Carbon Fiber Reinforced Boron Phenolic Resin Composites, Compos Part B-Eng, 221, 2021, 109011.
20.SHEN, L., LIU, L., WU, Z., Tensile Mechanical Behaviors of High Loading of Carbon Nanotube/ Epoxy Composites via Experimental and Finite Element Analysis, ADV ENG MATER, 22, 2019, 1900895.
21.MA, X., YUAN, H., ZHANG, H., Preparation, Characterization and Application of Sulfonated Meso-porous Hollow Carbon Microspheres, J Porous Mat, 26, 2018, 1103-1110.
22.SALIMIAN, S., ZADHOUSH, A., Water-glass Based Silica Aerogel: Unique Nanostructured Filler for Epoxy Nanocomposites, J Porous Mat, 26, 2019, 1755-1765.
23.KRIEG, A. S., KING, J. A., ODEGARD, G. M.,LEFTWICH, T. R., ODEGARD, L. K., FRALEY, P. D., MISKIOGLU, I., JOLOWSKY, C., LUNDBLAD, M., PARK, J. G., LIANG, R., Mechanical Properties and Characterization of Epoxy Composites Containing Highly Entangled As-Received and Acid Treated Carbon Nanotubes, NANOMATERIALS-BASEL, 11, 2021, 2445.
24.SHIRODKAR, N., CHENG, S., SEIDEL, G. D., Enhancement of Mode I Fracture Toughness Properties of Epoxy Reinforced with Graphene Nanoplatelets and Carbon Nanotubes, Compos Part B-Eng, 224, 2021, 109177.
25.SHIMAMOTO, D., TOMINAGA, Y., IMAI, Y., HOTTA, Y., Fiber Orientation and Flexural Properties of Short Carbon Fiber/epoxy Composites, J Ceram Soc Jpn, 124, 2016, 125-128.

26.MECHIN, P. Y., KERYVIN, V., GRANDIDIER, J. C., Effect of the Nano-filler Content on the Compressive Strength of Continuous Carbon Fibre/epoxy Matrix Composites, Compos Part B-Eng, 224, 2021, 109223.
27.GUVEN, I., CINAR, K., Micromechanical Modeling of Particulate-filled Composites Using Micro-CT to Create Representative Volume Elements, Int J Mech Mater Des, 15, 2019, 695-714.
28.CINAR, K., ERUSLU, S. O., DALMIS, I. S., GUVEN, I., Effect of Particle Shape on the Wear and Friction Behavior of Particle-reinforced Epoxy Coatings, J Coat Technol Res, 16, 2019, 1435-1445.
29.UMAIR, M., HUSSAIN, M., ABBAS, Z., SHAKER, K., NAWAB, Y., Effect of Weave Architecture and Glass Microspheres Percentage on the Low Velocity Impact Response of Hemp/green Epoxy Composites, J Compos Mater, 55, 2021, 2179-2195.
30.MEGAHED, M., FATHY, A., MORSY, D., SHEHATA, F., Mechanical Performance of Glass/epoxy Composites Enhanced by Micro- and Nanosized Aluminum Particles, J Ind Text, 51, 2019, 68-92.
31.N, B. Y., R, Z. S., P, H., Effect of Nano-SiO_2 Particles-silane Synergistic Modification on Mechanical Properties and Creep Properties of Basalt Fiberepoxy Composites, Acta Materiae Compositae Sinica, 39, 2022,
32.DING, J., YE, F., LIU, Q., YANG, C., GAO, Y., ZHANG, B., Co-continuous Hollow Glass Microspheres/epoxy Resin Syntactic foam Prepared by Vacuum Resin Transfer Molding, J Reinf Plast Comp, 38, 2019, 896-909.
33.DING, J., LIU, Q., YE, F., ZHANG, H., GAO, Y., ZHANG, B., Compressive Properties of Co-continuous Hollow Glass Microsphere/epoxy Resin Syntactic Foams Prepared Using Resin Transfer Molding, J Reinf Plast Comp, 39, 2020, 132-143.
34.WANG, S., CAO, M., XUE, H., CONG, F., LI, X., ZHAO, C., SU, W., Nano-silica Reinforced Epoxy Resin/nano-rubber Composite Material with a Balance of Stiffness and Toughness, High Perform Polym, 33, 2021, 685-694

Manuscript received: 21.06.2022